Regional Influences of Natural External Forcings on the Transition from the Medieval Climate Anomaly to the Little Ice Age

HEATHER J. ANDRES AND W. R. PELTIER

University of Toronto, Toronto, Ontario, Canada

(Manuscript received 25 August 2015, in final form 25 April 2016)

ABSTRACT

Reconstructions of historical climate changes indicate that surface air temperatures decreased over the preindustrial last millennium. Conflicting explanations have been proposed for the cause of the transition from the Medieval Climate Anomaly (MCA) in the early part of the last millennium to the Little Ice Age (LIA) near its end. The possible causes include volcanic emissions, total solar irradiance (TSI) variations, greenhouse gas concentration fluctuations, and orbital forcing variations. In the present paper, it is demonstrated that all of these climate forcings contribute significantly to simulated surface air temperature (SAT) and sea ice concentration changes over this period. On the other hand, simulated ocean heat content appears to respond significantly only to volcanic and TSI variations.

In model simulations at T85 spectral resolution, TSI reductions and volcanic emissions together generate significant increases in sea ice extent in the Barents Sea, which is found to be responsible for most of the temperature reductions over northwestern Europe. TSI appears less important to Arctic sea ice and SAT changes in simulations at T42 spectral resolution, which are weaker than at T85 resolution. Such resolution dependence is attributed to differences in background conditions in the responses to these external climate forcings. Nonlinearities in the forcing responses and sensitivities to background conditions challenge the assumption that sensitivity tests for given forcings can be run independently. Additionally, it is demonstrated that an ensemble of model simulations is required to isolate forcing responses even over a period as long as the last millennium.

1. Introduction

The preindustrial last millennium (years 850–1849 CE) is the most recent period dominated by natural sources of climate variability rather than anthropogenic sources (i.e., greenhouse gases and anthropogenic aerosols). Analyses of this period may provide insights into climate responses to natural external forcings, such as insolation and volcanic emissions. Historical reconstructions indicate that Northern Hemisphere (NH) surface air temperatures (SATs) exhibited substantial variations on centennial time scales superimposed on a secularly decreasing trend (Kaufman et al. 2009; Mann et al. 2009; Hanhijarvi et al. 2013; PAGES 2k Consortium 2013). Andres and Peltier (2013) have demonstrated that these features of NH SATs are well reproduced in a suite of

millennium simulations, as is the subsequent warming into the industrial period, when the influence of greenhouse gas forcings becomes more important.

The Medieval Climate Anomaly (MCA) encompasses a period of anomalous warmth during the early part of the last millennium. The Little Ice Age (LIA) corresponds to a period of anomalously low temperatures near the end of the millennium. Precise definitions for these periods vary between studies, but we choose years 950–1249 and 1450–1849 for the MCA and the LIA, respectively, following Masson-Delmotte et al. (2013). Explanations for the transition between these two periods have included long-term feedbacks in response to a succession of large volcanic eruptions (Zhong et al. 2011; Iwi et al. 2012; Schleussner and Feulner 2013; Schurer et al. 2014; McGregor et al. 2015), changes in orbital configuration and total solar irradiance (TSI) (Kaufman et al. 2009; Servonnat et al. 2010; Lehner et al. 2013; Phipps et al. 2013), and natural variations in greenhouse gases (GHGs) (Servonnat et al. 2010; Schurer et al. 2014). The goal of this study is to analyze the contributions of each of

Corresponding author address: Heather J. Andres, Department of Physics, University of Toronto, 60 Saint George St., Toronto ON M5S 1A7, Canada.
E-mail: handres@atmosp.physics.utoronto.ca

these external forcings to maps of simulated climate changes from the MCA to the LIA.

Large volcanic eruptions during the last millennium coincide with increased snow cover and glacier growth on Baffin Island (Miller et al. 2012) and a shift toward narrower North American (NAmer) tree rings (Gennaretti et al. 2014). However, because of the limited duration of explosive volcanic eruptions and the relatively short residence time of volcanic aerosols in the atmosphere, volcanic aerosols have been thought incapable of generating centennial-scale climate variations. Nevertheless, volcanic emissions from large eruptions have been shown to initiate multidecadal changes in ocean heat content (OHC), sea surface temperatures (SSTs), the Atlantic meridional overturning circulation (AMOC), and Arctic sea ice extent through a series of climate feedbacks and the thermal inertia of the oceans (Church et al. 2005; Gregory et al. 2006; Iwi et al. 2012; Schleussner and Feulner 2013; McGregor et al. 2015). These multidecadal responses are particularly long-lived if a sequence of large volcanic eruptions occurs before the climate has fully recovered from previous events (Zhong et al. 2011).

The success of atmosphere–ocean general circulation models at sustaining volcanic responses for centuries, as observed, depends on the accuracy of their representations of the orography and mean climate in high-latitude regions (Berdahl and Robock 2013). Such background climate conditions can have a strong influence on AMOC responses to large volcanic eruptions, resulting in volcanic climate responses either shorter than a decade or lasting many decades (Zhong et al. 2011; Mignot et al. 2011). Other model biases may also be important for generating long-lived responses to volcanic eruptions. Most models exaggerate the immediate climate effects of large volcanic eruptions, likely due to the specification of a single aerosol particle scattering radius (Timmreck et al. 2009, 2010; Gent et al. 2011). Additionally, most models underestimate internal ocean variability in comparison to observations (Gregory et al. 2006). Nevertheless, detection and attribution studies with both reconstructions and simulations point to an important role for large volcanic eruptions in the cooling from the MCA to the LIA (Schurer et al. 2014; McGregor et al. 2015).

The importance of volcanic eruptions to climate changes over the last millennium are obscured when examined over a longer period (Kaufman et al. 2009) and when regional and seasonal biases of proxy data sources are considered (Phipps et al. 2013). For example, orbital forcing alone has been found to generate the best agreement between simulated and reconstructed NH summer SAT variations in the extratropics (Phipps et al. 2013). Steadily decreasing trends have been observed

over the last millennia in northeast North Atlantic (NAtl) annual SST reconstructions (Cunningham et al. 2013) and in reconstructed Arctic summer SATs (Kaufman et al. 2009). The Arctic summer SAT trends have been attributed to the changing precessional component of orbital insolation (Kaufman et al. 2009) and are also present in the data generated for this study, as shown by Fig. 1b. Only during the early part of the twentieth century do high-latitude temperature reconstructions depart significantly from orbitally induced trends (Kaufman et al. 2009; Cunningham et al. 2013).

Multidecadal TSI and GHG variations acting together have been shown to be sufficient to generate LIA periods similar to those in NH reconstructions (Servonnat et al. 2010; Lehner et al. 2013). However, both of these model studies employ TSI reconstructions that exhibit relatively large variations between the Maunder Minimum and present day. Such large TSI variations have been shown to be inconsistent with reconstructed NH temperature variations over the last millennium (Schurer et al. 2014). Nevertheless, Lehner et al. (2013) identify two mechanisms whereby sustained decreases in radiative forcing (whether volcanic or solar in origin) may generate centennial-scale NH temperature reductions with amplified effects over northern Europe as observed.

GHGs have also been demonstrated to play an important role during the latter half of the last millennium (Servonnat et al. 2010; Schurer et al. 2013, 2014). In particular, a reduction in GHGs during the seventeenth century has been associated with detectable decreases in NH SATs (Schurer et al. 2013, 2014).

Finally, certain modes of internal variability, including El Niño–Southern Oscillation (ENSO), the North Atlantic Oscillation, the Pacific decadal oscillation, and the Atlantic multidecadal oscillation (AMO), are thought to have preferentially occupied particular states during the MCA and the LIA (e.g., Mann et al. 2009; Trouet et al. 2009). However, models have shown limited success at recreating those behaviors (Andres and Peltier 2013; Fernandez-Donado et al. 2013; Landrum et al. 2013).

In this study, the importance of the different external forcings to various geographic regions in the NH is examined over the last millennium. These analyses employ a suite of perturbation experiments described in section 2, and the results are presented in section 3. Finally, the implications of the regional importance of these forcings are discussed in section 4.

2. Experimental design

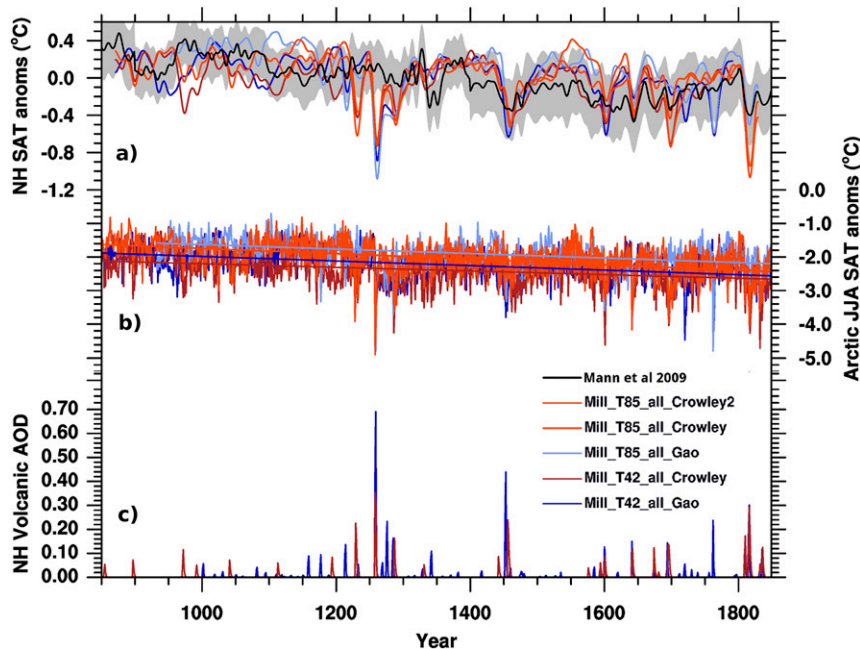The Community Climate System Model, version 3 (CCSM3; Collins et al. 2006), was employed to generate

FIG. 1. (a) NH annual SAT anomalies with respect to years 1250–1449 from the difference between fully transient preindustrial millennium simulations and a polynomial fit to control data. Simulated temperature anomalies are smoothed with a Gaussian filter ($\sigma = 4.0$). Mann et al. (2009) anomalies with respect to the same period, including gray shading for 95% confidence bounds. (b) Unsmoothed Arctic summer SAT anomalies with respect to control polynomials and showing trend lines. Colors are defined in the legend for (a),(b). (c) NH-averaged volcanic aerosol optical depths for Gao et al. (2008) (blue) and Crowley et al. (2008) (red).

all of the datasets presented here. Boundary conditions were consistent with the last millennium experiment of the Paleoclimate Modelling Intercomparison Project phase 3 (PMIP3; Schmidt et al. 2011, 2012). An overview of the simulations is presented in Table 1. There are five

fully transient millennium simulations, two at a spectral resolution of T42 and three at T85. Two different volcanic reconstructions have been employed at each resolution [i.e., those from Gao et al. (2008) and Crowley et al. (2008)], and in all analyses presented herein either

TABLE 1. Specifications of control and fully transient simulations, as well as each perturbation experiment. Number indicates the total number of simulations. Start and end specify the simulation duration in Common Era (CE) calendar years. Initial point indicates the control or fully transient simulation year when each experiment is initialized. TSI, orbital, and GHG refer to specific forcings, where F indicates fixed forcings, with the fixed date (CE year) in parentheses and T for transient forcings. Transient volcanic forcings listed as either Gao or Crowley are for Gao et al. (2008) or Crowley et al. (2008) reconstructions, respectively. Transient TSI forcings are from Vieira et al. (2011). Transient orbital forcings are enacted through the Berger (1978) scheme internal to CCSM3 through a code modification developed by B. Briegled and B. Kauffman (N. Rosenbloom 2009, personal communication). Transient GHG forcings are from Joos and Spahni (2008).

Experiment	Number	Start	End	Initial point	Volcanic	TSI	Orbital	GHG
Mill_T42_ctl	1	2940	3940	—	None	F (850)	F (850)	F (850)
Mill_T85_ctl	1	2150	3150	—	None	F (850)	F (850)	F (850)
Mill_T42_all_Gao	1	850	1849	2940	Gao	T	T	T
Mill_T42_all_Crowley	1	850	1849	2940	Crowley	T	T	T
Mill_T85_all_Gao	1	850	1849	2150	Gao	T	T	T
Mill_T85_all_Crowley	1	850	1849	2150	Crowley	T	T	T
Mill_T85_all_Crowley2	1	850	1849	2153	Crowley	T	T	T
NO_GHG	1	850	1849	850	Gao	T	T	F (850)
NO_ORBIT	1	850	1849	850	Crowley	T	F (850)	T
NO_VOLC	5	1200	1499	1200	None	T	T	T
NO_TSI	5	1200	1499	1200	Both	F (1200)	T	T

Gao or Crowley is appended with an underscore to simulation labels identifying which reconstruction was used. Finally, Mill_T85_all_Crowley2 is forced identically to Mill_T85_all_Crowley, but it is initialized three years later in the control run. Further discussion of the fully transient simulations can be found in Andres and Peltier (2013, 2015).

Four experiments have been initialized from the fully transient simulations. In each experiment, simulations are produced with one forcing held fixed to its value at the branching point. When the volcanic forcing is held fixed, no eruptions are prescribed for the duration of the perturbation simulation. This method prevents discontinuities in any of the time series while permitting an examination of the full influence of each forcing, including its interaction effects with the other forcing responses. These experiments are named according to the boundary condition held fixed (i.e., NO_GHG, NO_ORBIT, NO_VOLC, and NO_TSI) and are defined in Table 1 and described in more detail below.

Fully transient and perturbation time series have been corrected for disequilibration by subtracting a third-order polynomial fit to corresponding data from the control simulation. The control simulation equilibration criteria applied in this study are conservative and are described in Andres and Peltier (2013). Nevertheless, lingering disequilibration in the control simulation deep ocean appears to generate initial trends in control simulation OHC that coincide with variations in the transient simulations. Further details concerning this issue are provided in appendix A. Note that, because of irretrievable data loss, the polynomial fit to NH sea ice data was performed including decadally spaced annual values reconstructed from restart data.

Results are presented for simulated SATs, OHC (defined as the depth-integrated thermal energy carried by the water parcels after being returned to the surface adiabatically), and NH sea ice concentration. In addition, annual time series of the AMOC [defined following Tulloch and Marshall (2012) to be the meridional streamfunction average at depths of 500–1800 m between 35° and 50°N] are presented. Changes from the MCA to the LIA are constructed by subtracting averages over each of these periods. Differences between changes from the MCA to the LIA in the fully transient simulations and in the perturbation experiments indicate external forcing responses. Where there is only a single perturbation experiment, only a single difference is calculated with respect to the corresponding fully transient simulation. Finally, the linearity of the responses is tested by comparing average fully transient changes to the sum over all of the average perturbation responses in each T42 Gaussian-grid cell.

A 95% significance criterion is applied to all results presented here. This significance is evaluated with respect to confidence intervals defined by bootstrapping control data. Consequently, these tests facilitate a separation of forced climate responses from those associated with internal variability alone. For the maps, significance is established separately in every grid cell based on confidence intervals determined for that grid cell. With these confidence limits, it is expected that one in every 20 grid cells will be significant by chance alone. Thus, significant regions are only discussed if they include many grid cells. The bootstrapping methods are described in more detail in appendix B.

a. NO_GHG

The NO_GHG experiment consists of one millennium-length T42 simulation initialized from the same point in the T42 control run as the fully transient simulations. This simulation is identical to Mill_T42_all_Gao except that trace gases are held fixed to year 850 values. Reconstructed greenhouse gas radiative forcings over the preindustrial millennium are plotted in Fig. 2a and exhibit slow variations of low amplitude until the seventeenth century. Even then, the variations are of small amplitude in comparison with those during the twentieth century (not shown). The changes in GHG forcing from the MCA to the LIA are insignificant, and the seventeenth century includes the only pronounced negative values.

b. NO_ORBIT

The NO_ORBIT experiment consists of a single millennium-length T42 simulation. Its forcings are identical to Mill_T42_all_Crowley, except that the orbital forcing is fixed to year 850 values. Orbital changes over the last millennium are generated by a combination of changes in eccentricity, obliquity, and precession and affect the insolation at the top of Earth's atmosphere through a multiplicative factor. Eccentricity describes how elongated Earth's orbit around the sun is and thus the degree of contrast in the insolation received during different seasons. The eccentricity varies with a dominant period of approximately 100 ka (1 ka = 1000 yr), so its changes during the last millennium are small. Precession alters the time in the year when Earth is closest to the sun (at its perihelion) with periods of approximately 20 ka. Since seasons in the Northern and Southern Hemispheres are out of phase, the effects on seasonal contrasts of precessional shifts differ in the two hemispheres. Over the last millennium, precession changes shifted the timing of the perihelion by 18 days through the December solstice. Finally, obliquity changes affect the angle of Earth's rotation axis with
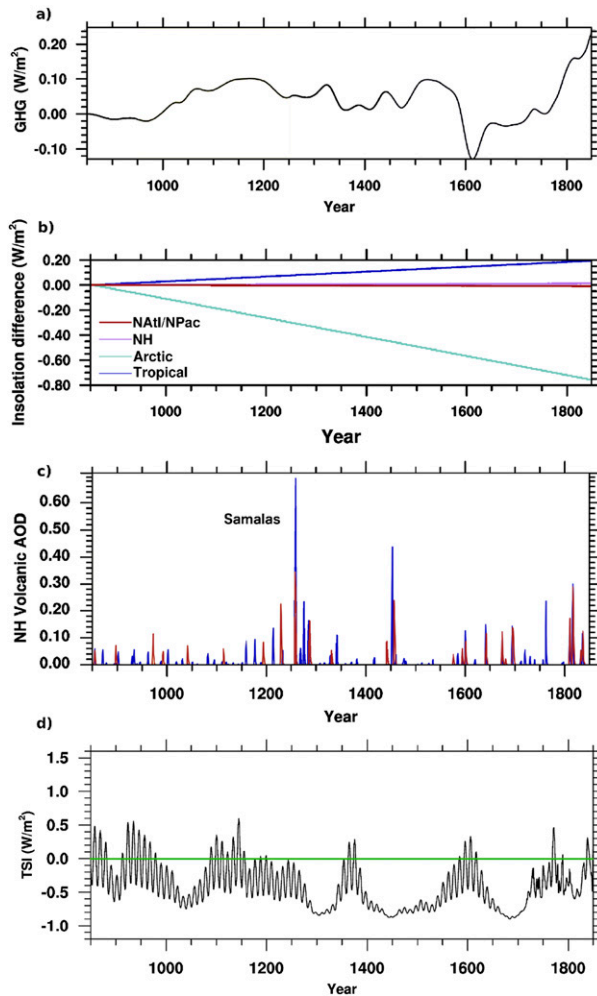
FIG. 2. Radiative forcings with respect to their values at year 850 for (a) GHG and (b) orbital boundary conditions. (c) Volcanic aerosol optical depth, where blue lines correspond to Gao et al. (2008) and red lines correspond to Crowley et al. (2008). (d) TSI radiative forcing with respect to the value in year 1200, which is marked by a green line.

respect to the plane of its orbit about the sun with a period of approximately 41 ka. Obliquity decreased throughout the last millennium, thereby reducing contrasts between the seasons in both hemispheres.

Orbital configuration changes affect regional insolation more strongly than global totals. Annually averaged insolation differences with respect to year 850 values are plotted in Fig. 2b for the tropics, Arctic, NH, and NAtl and North Pacific (NPac) regions. Annual insolation changes from the MCA to the LIA are only significant in the Arctic and the tropics. Since polar regions receive very little insolation during their winters, their annual insolation totals are relatively insensitive to changes during winter and highly sensitive to changes during summer. Thus, on an annually

averaged basis, Arctic insolation decreases over the millennium by $-0.75 \, \mathrm{W \, m^{-2}}$ (or -0.4%), with reductions as high as $-4.4 \, \mathrm{W \, m^{-2}}$ during the summer. The tropics are not very sensitive to obliquity changes, and precessional shifts over the last millennium increase the insolation during DJF and decrease it during JJA. The net annual effect is that tropical insolation increases linearly by $0.20 \, \mathrm{W \, m^{-2}}$ over the millennium. However, peak increases and decreases are 3.5 and $-3.4 \, \mathrm{W \, m^{-2}}$ during MAM and SON, respectively, when the tropics align most directly with incoming solar radiation.

c. NO_VOLC

There are five NO_VOLC simulations, each initialized from year 1200 in a different fully transient simulation. Each perturbation simulation is identical to the one from which it was initialized, except that there are no volcanic emissions. Because of the strength of variability on annual time scales in the volcanic datasets, these simulations only cover years 1200–1499, thereby including 50 years in each of the MCA and LIA (termed short MCA and short LIA). This period captures two major sequences of substantial volcanic activity, as shown in Fig. 2c. The largest eruption of the millennium, which is attributed to the Samalas volcano (Lavigne et al. 2013), occurs immediately following the MCA and is succeeded by several others within 50 years. The next largest eruption, which is attributed to Kuwae, occurs at the start of the LIA. The NO_VOLC simulations do not continue into the seventeenth century, when large eruptions occur quasi regularly until the end of the millennium.

d. NO_TSI

There are five NO_TSI experiments initialized from year 1200 in each of the fully transient simulations. These runs are forced identically to the original simulations except that the TSI is held constant at year 1200 values. The TSI time series is plotted with respect to its values in the year 1200 in Fig. 2d. Years 1200–1499 are sufficient to extract substantial TSI variation, including two periods each of relatively high and low values, with high TSI occurring early in the thirteenth century and late in the fourteenth century and low TSI occurring in between those periods and in the fifteenth century (i.e., the Wolf and Spörer Minimums). Consequently, TSI averages are significantly larger in the short MCA than the short LIA, although they are negative with respect to year 1200 values during all of the periods.

3. Results

Maps of changes from the MCA to the LIA (or short MCA to the short LIA, where applicable) are discussed
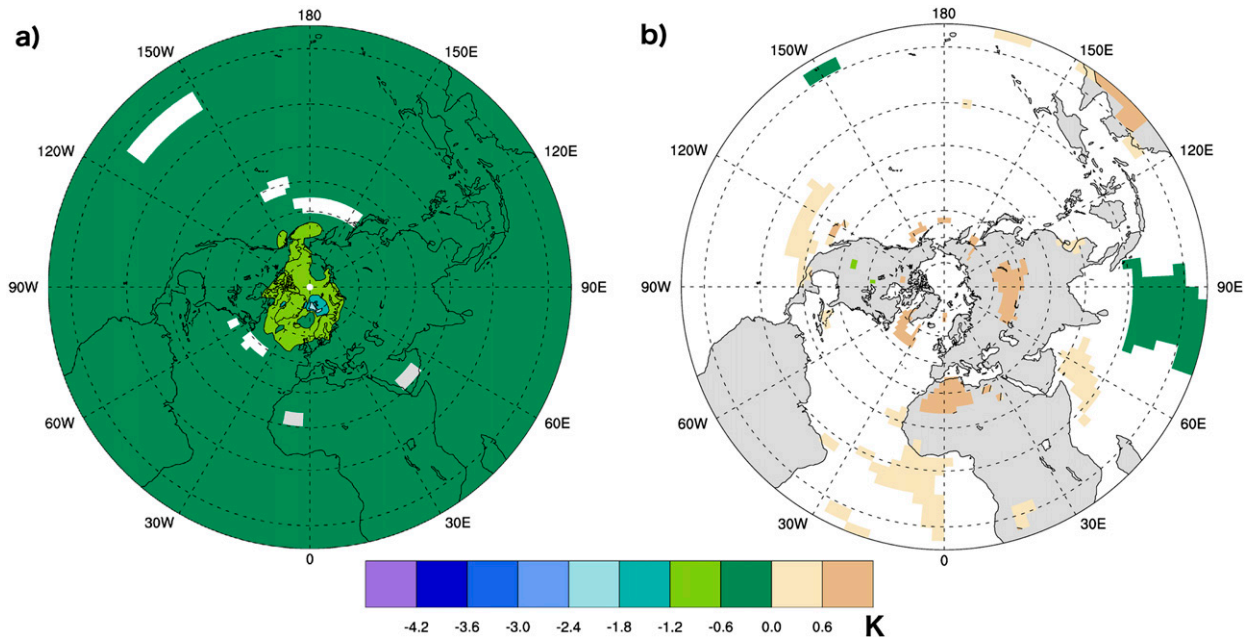
FIG. 3. (a) T42 simulation ensemble-average SAT changes from the MCA to the LIA. (b) Differences between average changes from the short MCA to the short LIA for T42 simulations and the linear combination of average changes associated with each forcing. Only values significant at $p < 0.05$ with respect to control simulation variations in each grid cell are shown.

in the following subsections for SATs, OHC, and sea ice concentration. Where experiments include multiple perturbation simulations, ensemble averages are presented. Otherwise, plotted differences are based on single simulations alone.

a. Surface air temperatures

Simulated, smoothed SATs averaged over the NH are plotted in Fig. 1a with a multisensor reconstruction of NH temperatures from Mann et al. (2009) in black. The SATs are defined as anomalies with respect to years 1250–1449, and the simulations have been smoothed to match the standard deviation of the Mann et al. (2009) reconstruction over the MCA (when there are few large volcanic eruptions). The simulations lie within the 95% confidence bounds of the reconstruction over most of the preindustrial millennium. The most prominent exceptions occur during large volcanic eruptions, when simulated SAT variations are significantly larger than reconstructed SATs. The amplitude of the simulated change in NH SATs from the MCA to the LIA is smaller than in the Mann et al. (2009) reconstruction. However, the amplitude of this reconstructed change has been found to depend strongly on the reconstruction method employed and the quality of the data included in the analysis (Wang et al. 2015). The ensemble average of global SAT changes between the MCA and LIA as defined by Wang et al. (2015) (i.e., years 950–1249 and

1400–1699) is 0.08 ± 0.02 K for the simulations presented here. This value places these simulations at the low end of PMIP3 simulations and within the range spanned by different reconstruction methods using the Past Global Changes (PAGES) 2k Consortium dataset (Wang et al. 2015).

Maps of significant ($p < 0.05$) ensemble-average SAT changes from the MCA to the LIA are presented in Fig. 3a for T42 simulations and Fig. 4a for T85 simulations. Positive changes indicate more positive values during the LIA, and negative values indicate more positive values during the MCA. The transient simulations exhibit a general cooling from the MCA to the LIA that is strongest in the Arctic and in the Greenland and Barents Seas in particular. The peak amplitude of these differences is larger at T85 resolution.

The contribution of each forcing to MCA–LIA changes is presented in terms of the difference between fully transient and perturbation experiments. Such perturbation differences for T42 simulations are plotted in Fig. 5, and perturbation differences for T85 simulations are plotted in Figs. 4b,c. Negative values indicate that there is greater cooling from the MCA to the LIA when the perturbation variable varies than when it is fixed. All of the forcings exhibit regions of significant values, but the regions of significance are more extensive for NO_VOLC and NO_TSI. The greater significance of differences with respect to those two experiments can be
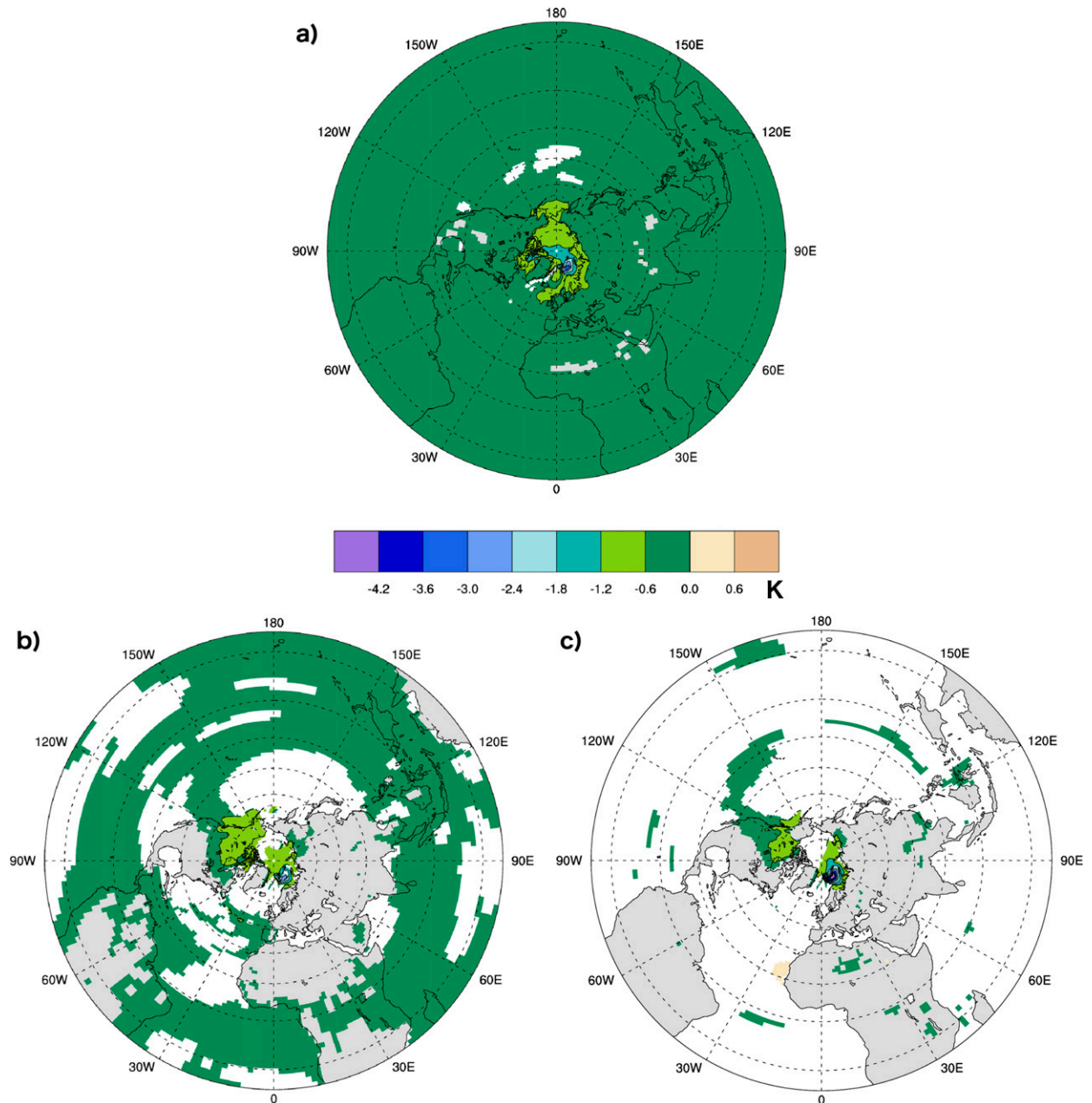
FIG. 4. (a) T85 simulation ensemble-average SAT changes from the MCA to the LIA. Average differences between fully transient changes from the short MCA to the short LIA and the (b) NO_VOLC and (c) NO_TSI experiments. Only values significant at $p < 0.05$ with respect to control simulation variations in each grid cell are shown.

partly explained by the larger numbers of perturbation simulations. Nevertheless, differences between each NO_VOLC simulation and its corresponding fully transient run exhibit more extensive regions of significance than do either the NO_GHG or NO_ORBIT differences.

None of the perturbation differences at T42 resolution exhibit significant signals over the Arctic, which is the region of strongest SAT change from the MCA to the LIA. In contrast, both NO_VOLC and NO_TSI perturbation differences at T85 resolution are associated with significant reductions from the short MCA to the short LIA in the Barents Sea. Both of these signals are similar in amplitude to the fully transient change in this region. Since neither GHG nor orbital forcings are expected to generate increases in Arctic SATs over the
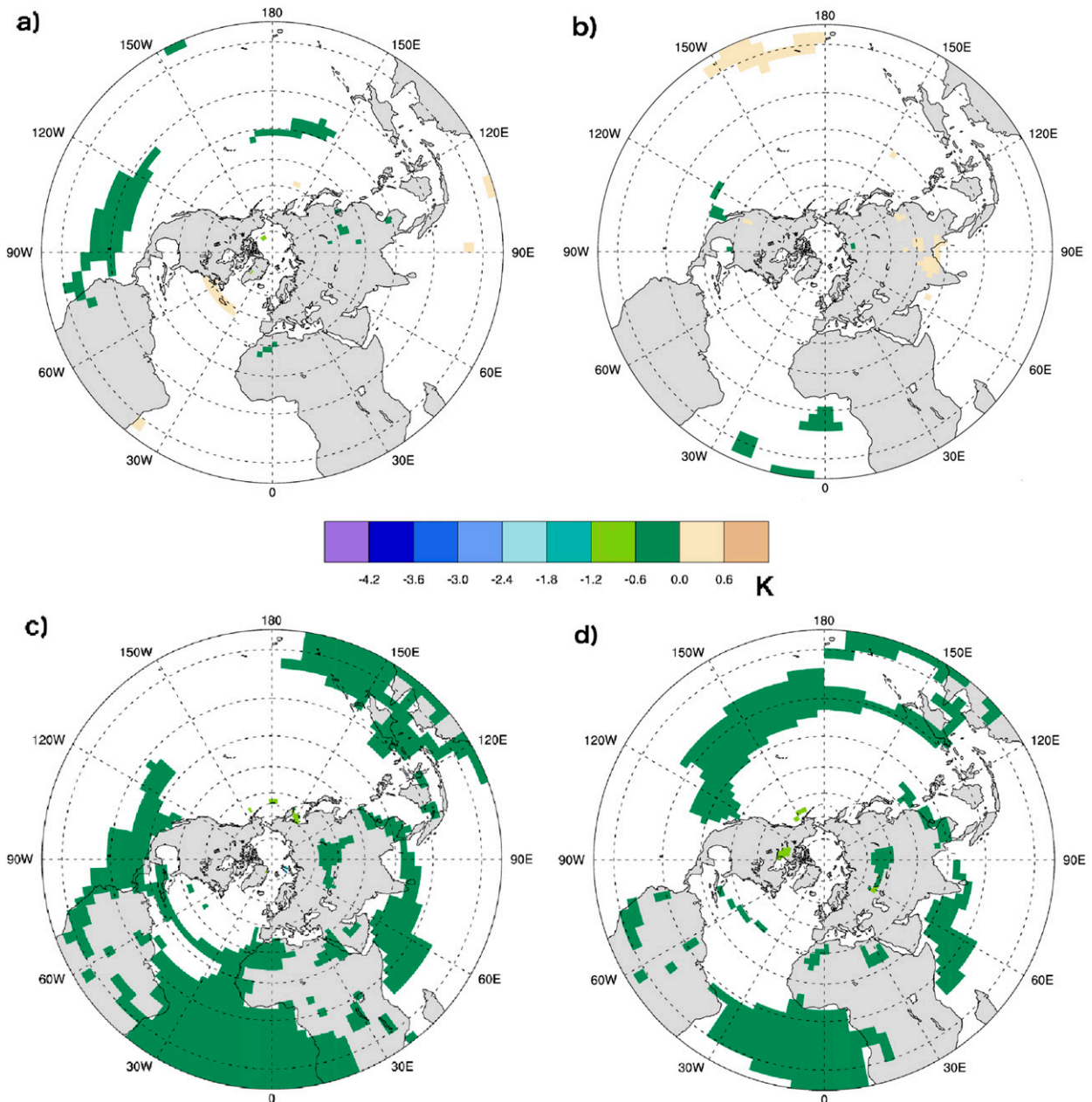
FIG. 5. Differences between SAT changes from the MCA to the LIA for T42 simulations with all forcings transient and the (a) NO_GHG and (b) NO_ORBIT experiments. Differences in T42 SAT changes from the short MCA to the short LIA for (c) NO_VOLC and (d) NO_TSI experiments. Differences are based on single perturbation experiments in (a) and (b) and averages over all T42 experiments in (c) and (d). Only values significant at $p < 0.05$ with respect to control simulation variations in each grid cell are shown.

last millennium, the strength of the NO_TSI and NO_VOLC signals suggests that both forcings are required in order to capture the fully transient SAT response in the Barents Sea. This suggests a degree of nonlinearity in the SAT response in this region.

The tropics exhibit the most extensive regions of significant perturbation SAT differences. Both the TSI and the volcanic forcings affect SAT changes from the short

MCA to the short LIA in the tropical Pacific and Atlantic, although their response patterns differ and vary with resolution. At both resolutions, TSI is responsible for a cooling along the southern branch of the North Pacific Gyre and cooling in the tropical Atlantic. Its significant signals are more extensive at T42 resolution. GHGs are only associated with significant changes in the tropical Pacific. Both volcanic and GHG forcings are
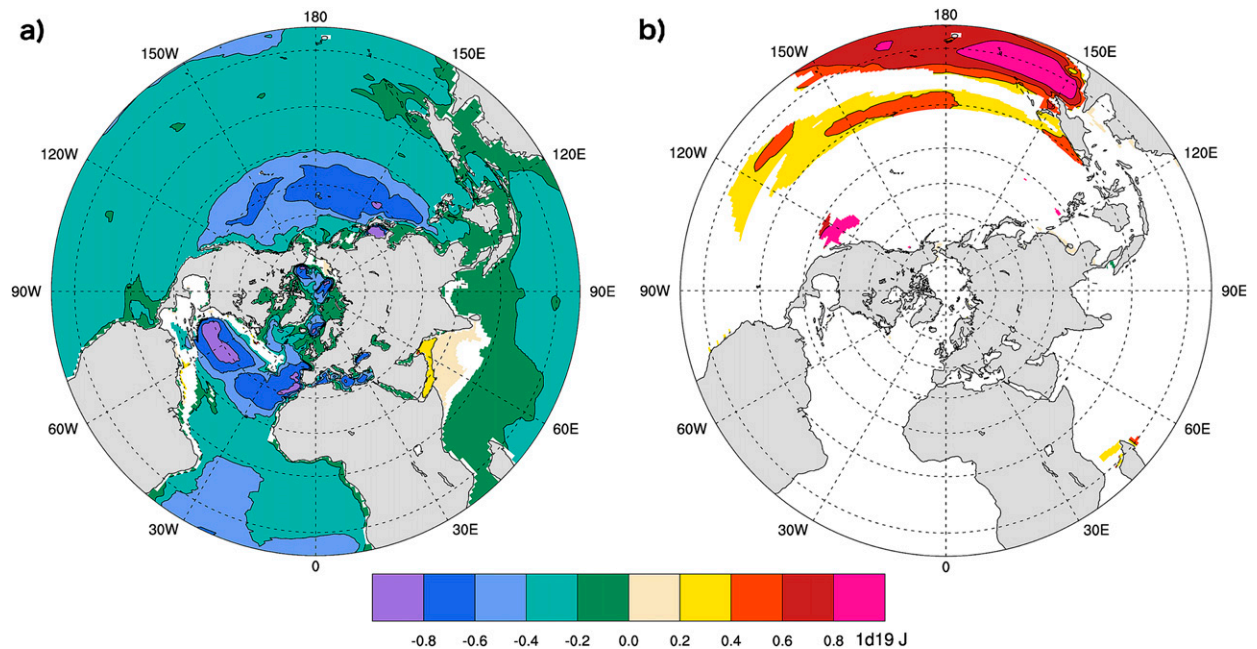
FIG. 6. As in Fig. 3, but for OHC changes (10^{19} J) at T42 resolution.

associated with cooling in the location of the Equatorial Counter Current, although significant signals are restricted to the eastern side of the Pacific basin at T42 resolution. Finally, orbital changes are associated with significant warming over the western tropical Pacific and patches of significant cooling over the tropical Atlantic.

b. Ocean heat content

OHC ensemble-average changes are plotted in Figs. 6a and 7a. MCA OHC values are larger than LIA values over most of the NH, with the exception of the Indian Ocean. There, OHC values increase during the preindustrial millennium in simulations at both resolutions, with more extensive increases at T85 resolution. OHC reductions have the largest amplitude in the midlatitudes and in the NAtl basin. The strength of the NAtl midlatitude change is similar at both resolutions, but in most other regions the change at T42 resolution is more negative than the change at T85 resolution.

The largest resolution contrast in OHC changes from the MCA to the LIA is in the Arctic, where there are strong reductions at T42 resolution and a mixture of weaker (but still significant) increases and decreases at T85 resolution. Resolution dependence in Arctic OHC differences is particularly evident when examining time series of regional averages for different ensemble members. In Fig. 8, average Arctic OHC values decrease strongly by the end of the millennium in T42 simulations and are characterized by minor fluctuations with no overall secular tendency in the T85 simulations. Since

the resolution of the ocean and sea ice model components are the same for both T42 and T85 model configurations, the differences between the responses must be due to differences in the coupled climate and/or atmospheric responses to the forcing. Finally, there are strong contrasts based on resolution in the North Pacific, where T42 simulations exhibit peak decreases in the midlatitudes, and T85 simulations exhibit little variation by latitude.

Perturbation OHC differences for NO_GHG and for NO_TSI at T85 resolution are insignificant in nearly all grid cells, so they are not shown in Figs. 9 and 7. Orbital forcing exhibits a small region of increased OHC in the Labrador Sea and subpolar NAtl. In contrast, both volcanic and TSI forcings are important to OHC reductions in Pacific low latitudes at T42 resolution. These changes are also apparent in tropical OHC averages plotted in Fig. 10b. Additionally, volcanic forcing responses at both resolutions exhibit strong, localized cooling along the southeastern margin of the North Atlantic.

c. Northern Hemisphere sea ice concentrations

Finally, NH sea ice concentrations plotted in Figs. 11a and 12a generally increase at both resolutions, although this increase is much stronger for T85 resolution than T42. Nevertheless, sea ice extent changes as delineated by the 15% concentration threshold (not shown) are similar for simulations at the two resolutions. Although sea ice changes at both resolutions exhibit strong
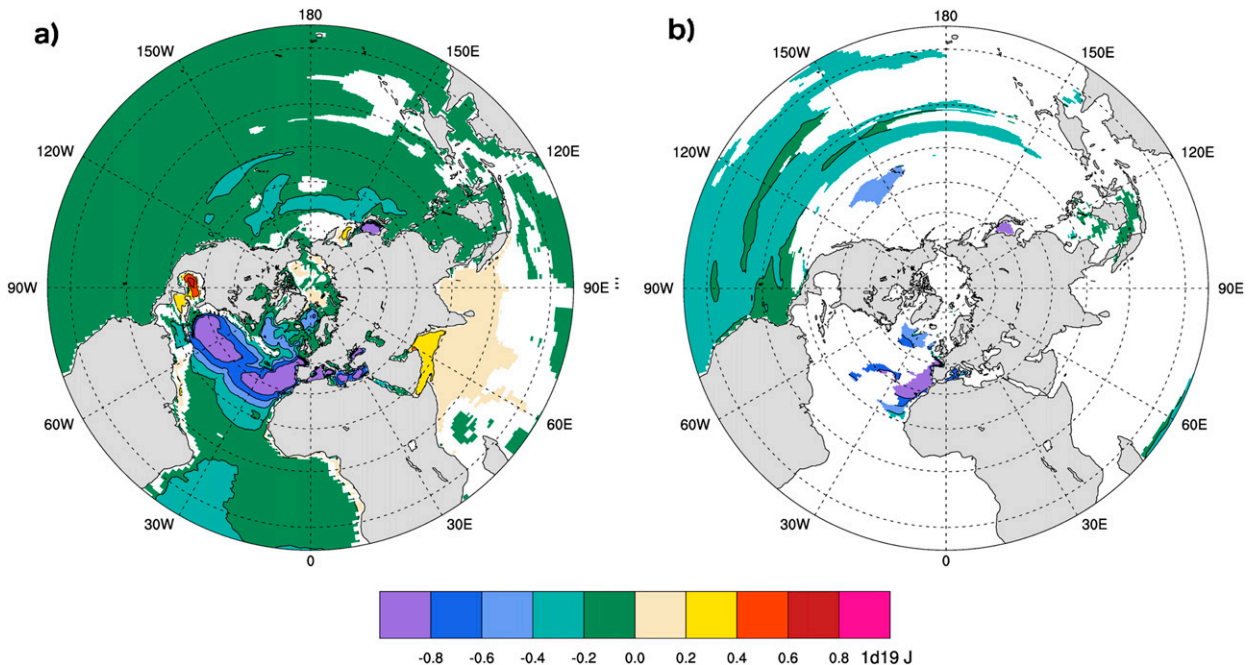
FIG. 7. (a) T85 simulation ensemble-average OHC changes (10^{19} J) from the MCA to the LIA. Average differences between fully transient changes from the short MCA to the short LIA and the (b) NO_VOLC experiment. Only values significant at $p < 0.05$ with respect to control simulation variations in each grid cell are shown.

increases in the Barents Sea, the locations of the other large changes differ. Most noticeably, the T85 simulations exhibit relatively strong sea ice growth in the Labrador Sea in comparison to the T42 simulations.

All perturbation variables are seen to contribute to NH sea ice concentration increases in Figs. 13 and 12b,c. Most of the increases occur along the sea ice margins of the NAtl and NPac, resulting in increases of sea ice extent. All variables contribute to significant sea ice increases in the Norwegian Sea, although GHG variations are associated with sea ice reductions in its northernmost part. Fixing either volcanic or TSI forcing results in the loss of much of the sea ice growth in the Gulf of Alaska at both resolutions. However, only volcanic forcings appear important to sea ice growth in the

Barents Sea in T42 simulations, whereas both volcanic and TSI forcings are associated with strongly significant increases in sea ice concentration there at T85 resolution.

d. Response additivity

The linearity of the forcing responses is estimated by calculating the differences between fully transient changes from the short MCA to the short LIA (not shown for NO_GHG and NO_ORBIT) and a linear combination of perturbation differences. The average of such calculations for Mill_T42_all_Gao and Mill_T42_all_Crowley is presented in Fig. 3b for SATs, Fig. 6b for OHC, and Fig. 11b for sea ice concentration. In regions with positive changes from the short MCA to the short
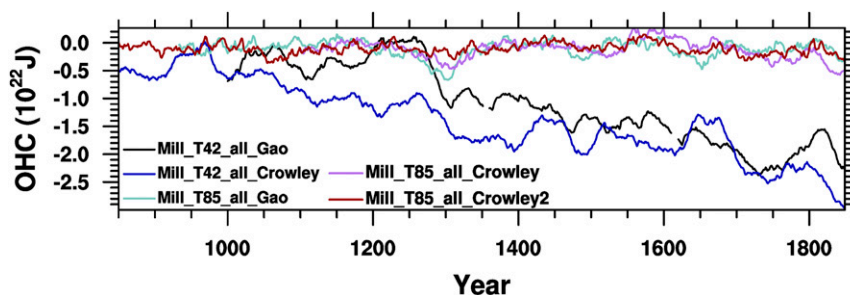

FIG. 8. Differences between OHC summed over the Arctic region and the control simulation polynomial fit for each of the fully transient simulations. Datasets are labeled in the legend.
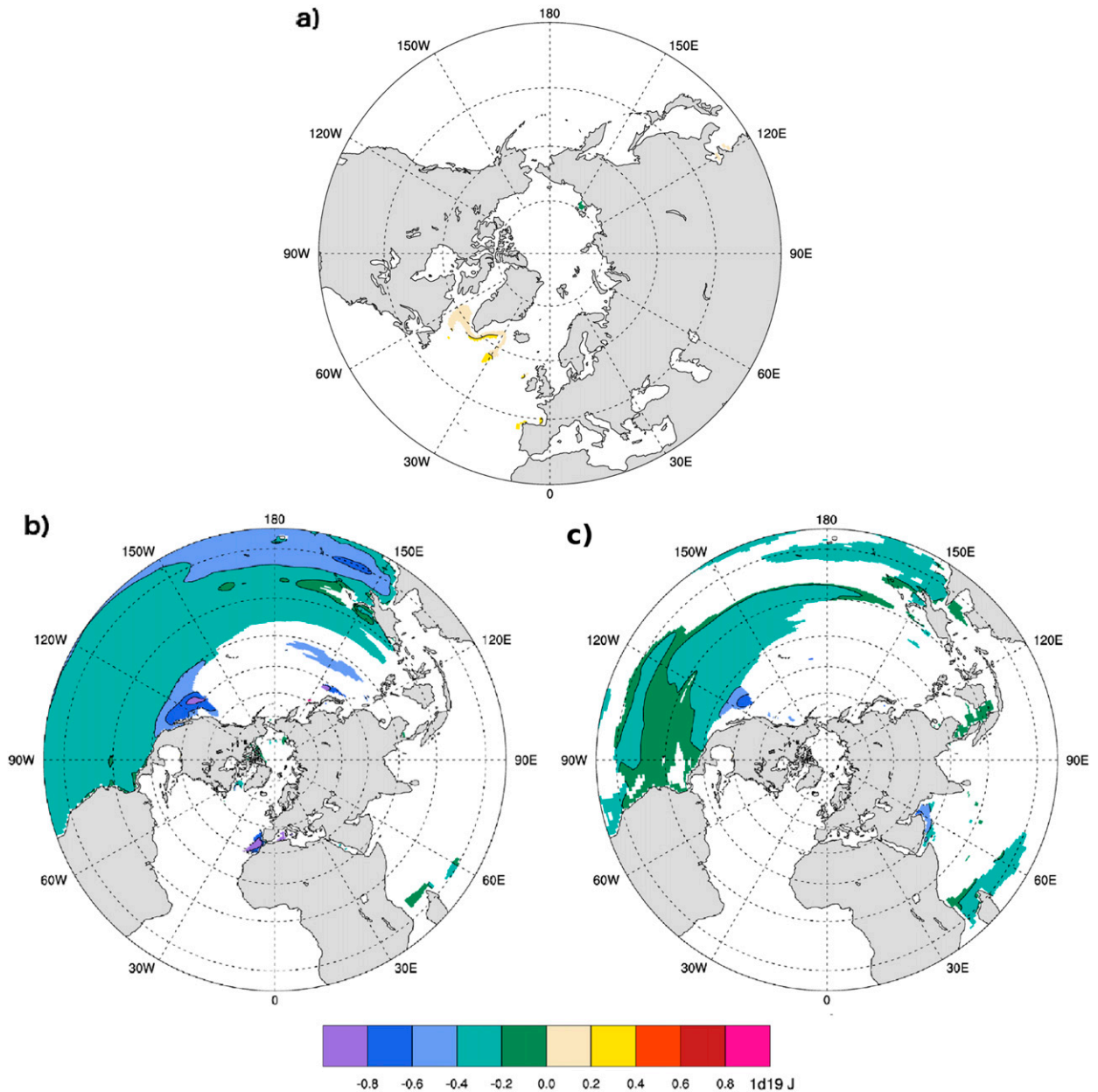
FIG. 9. Significant differences between OHC changes (10^{19} J) from the MCA to the LIA for T42 simulations with all forcings transient and the (a) NO_ORBIT experiment. Differences between the short MCA and short LIA for the (b) NO_VOLC and (c) NO_TSI experiments. Only values significant at $p < 0.05$ with respect to control simulation variations in each grid cell are shown.

LIA, positive values indicate an underestimation of fully transient changes by the linear combination. In regions with negative changes, positive values indicate an overestimation of the fully transient change by the linear combination.

Note that perturbation differences for NO_GHG and NO_ORBIT experiments are only calculated with respect to their corresponding fully transient simulations, so these values are identical in the two linear combinations. Such duplication increases the width of

the confidence interval for the linearity tests compared to a case with two separate simulations each for the NO_GHG and NO_ORBIT experiments. Thus, the confidence intervals applied to test the significance of nonlinear differences are estimated via bootstrapping by averaging over sets of two linear combinations with two of the randomly chosen summation terms in common.

SAT differences show the strongest overestimation by the linear combination in North Africa, central
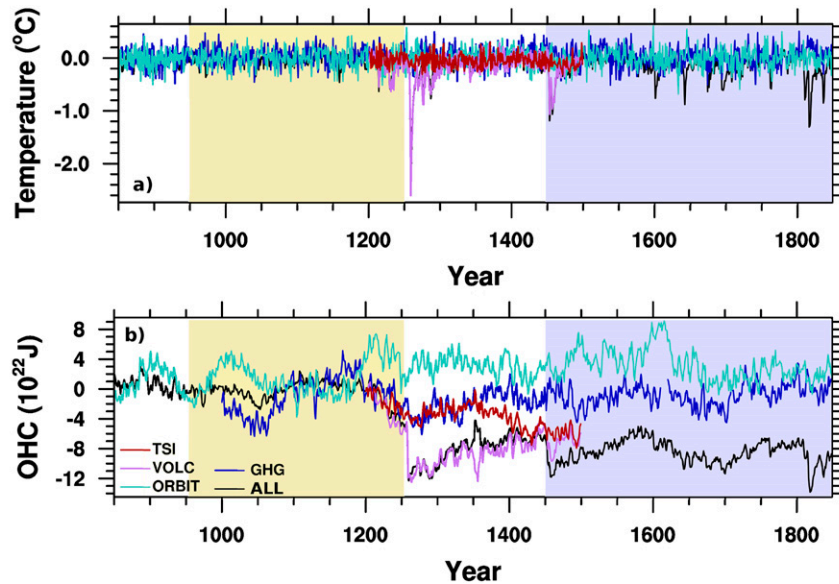
FIG. 10. T42 average perturbation differences in (a) averaged SAT and (b) summed OHC with respect to time over the tropical zone defined by ±20° latitude with respect to the equator. The yellow-shaded region corresponds to the Medieval Climate Anomaly, and the blue-shaded region corresponds with the Little Ice Age.

Eurasia, and the Labrador Sea. SAT changes in the eastern tropical Pacific Ocean are also overestimated. The linear combination underestimates short MCA–short LIA changes in the Indian Ocean. OHC differences are strongly overestimated in the western tropical Pacific Ocean. Finally, sea ice concentration changes are significantly overestimated in most of the regions of sea ice expansion into regions without previous sea ice cover.

4. Discussion

Since the LIA period chosen in this study includes both the most negative and most positive GHG
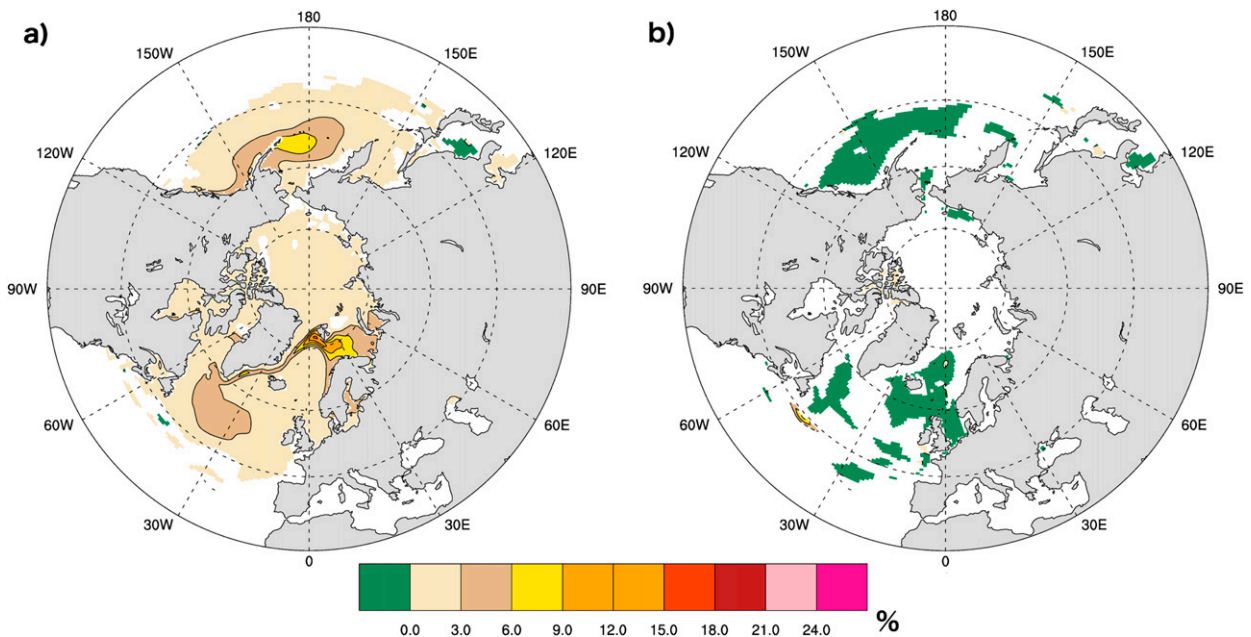

FIG. 11. As in Fig. 3, but for sea ice concentration changes at T42 resolution.
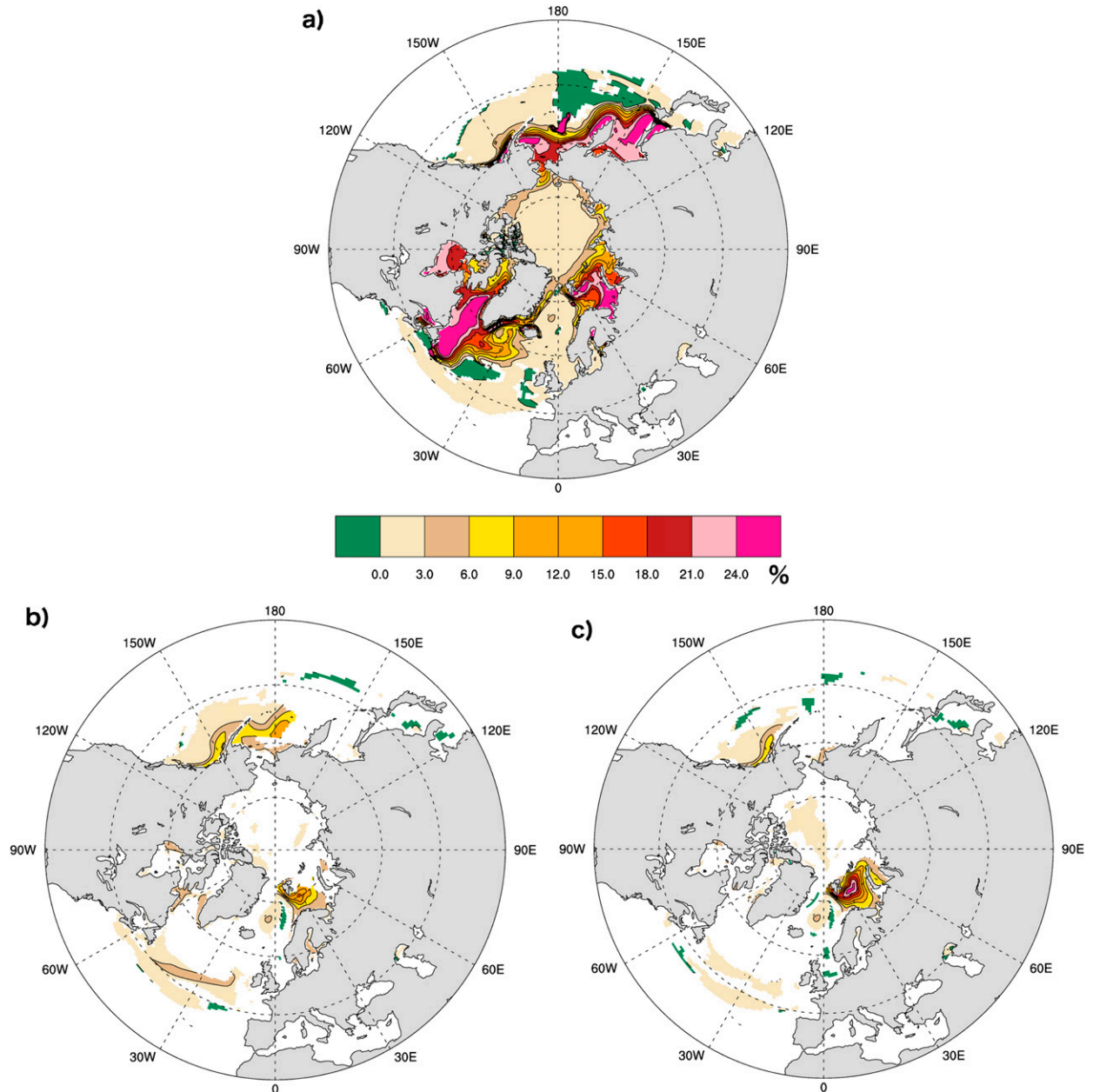
FIG. 12. (a) T85 simulation ensemble-average sea ice concentration changes from the MCA to the LIA. Average differences between fully transient changes from the short MCA to the short LIA and the (b) NO_VOLC and (c) NO_TSI experiments. Only values significant at $p < 0.05$ with respect to control simulation variations in each grid cell are shown.

radiative forcing values of the preindustrial last millennium, the strengths of the GHG responses are not well captured. For comparison, NO_GHG perturbative differences are calculated for SATs, OHC, and sea ice concentration in Figs. 14a, 14b, and 14c, respectively, for changes between the MCA and a period of low GHG radiative forcing values, years 1595–1644. The significance of these results is evaluated with respect to bootstrapped datasets of the same duration as the two

periods under examination. Regions with significant responses are more extensive for all variables, but most especially for SATs. GHG reductions are associated with general cooling over most of the tropics and subtropics and amplified cooling over the Arctic. Significant warming is detected in a few locations that are mostly in northern midlatitudes.

Our results point to three regions of particular importance to an understanding of forced climate changes
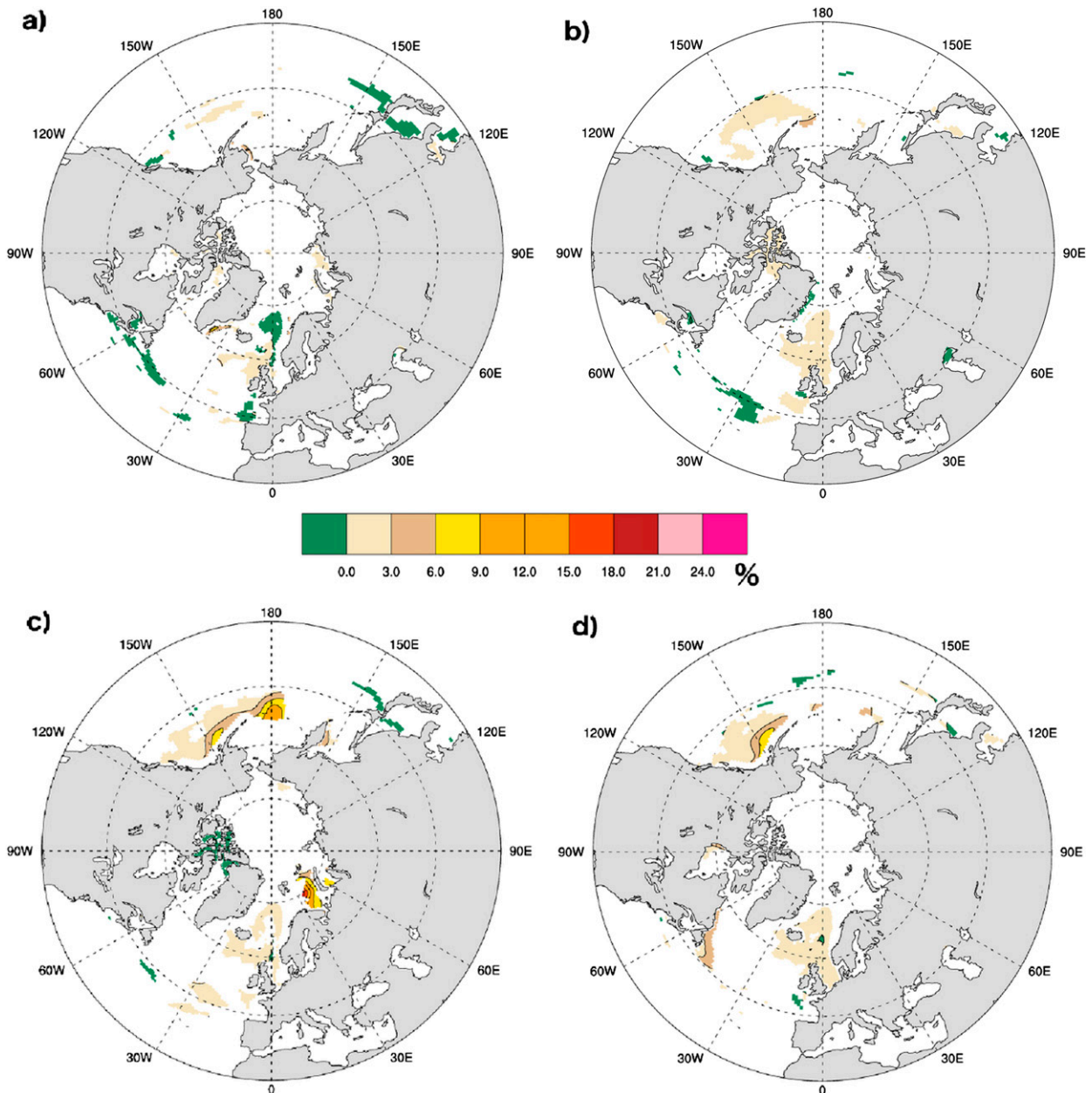
FIG. 13. As in Fig. 5, but for sea ice concentration perturbation differences at T42 resolution.

from the MCA to the LIA: namely, the tropical Pacific, the North Atlantic, and the Arctic.

Both tropical SATs and OHC exhibit strong responses to external forcings over the last millennium, but tropical OHC responses to even short-lived but strong forcings are sustained much longer because of the thermal inertia of the ocean's mixed layer. This integrative effect reduces the amplitude of OHC responses to short-lived forcings relative to background variability, but it also can increase the relative amplitude

of long-lived forcings. In Fig. 10b, the OHC perturbation differences averaged over the tropics (defined here to be within ±20° latitude with respect to the equator) experience much longer-lasting responses to volcanic eruptions than SATs in Fig. 10a do. OHC also exhibits more anomalous, gradual decreases in response to TSI reductions.

Significant tropical Pacific responses are collocated with the center of ENSO variability, but this collocation does not necessarily imply a dynamical ENSO response
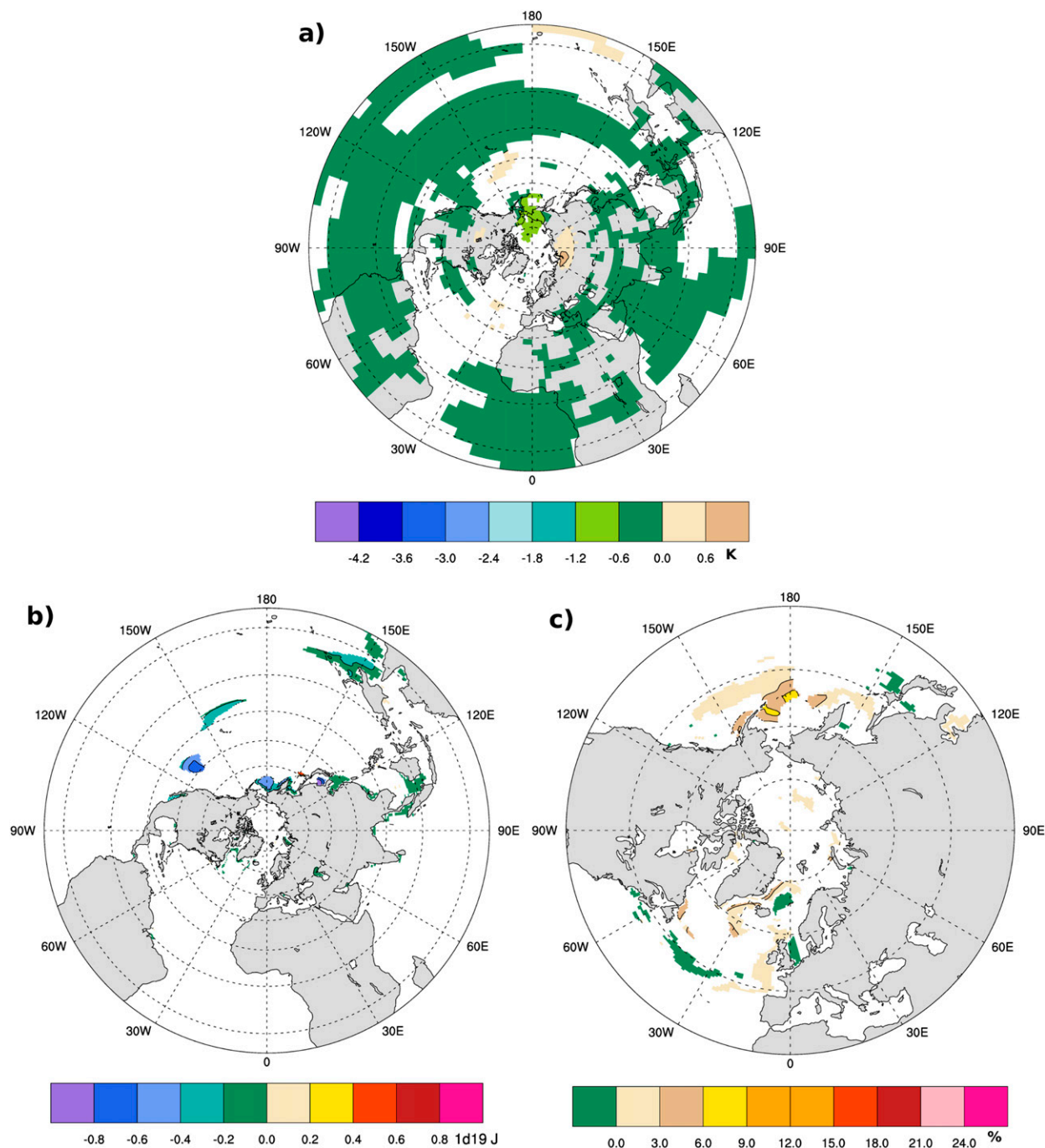
FIG. 14. Differences between fully transient and NO_GHG changes from the MCA to a period of low GHG forcing (years 1595–1644 CE) for (a) SATs, (b) OHC (10^{19} J), and (c) sea ice concentration. Only values significant at $p < 0.05$ with respect to control simulation variations over periods of similar length in each grid cell are shown.

is involved (van Loon and Meehl 2008). Our results suggest a shift toward more La Niña–like conditions over the preindustrial last millennium. These results disagree with one proxy-based reconstruction of historical ENSO variations (Mann et al. 2009). However,

the perceived shift to more positive ENSO states from the MCA to the LIA has been shown to depend on the reconstruction method employed (Wang et al. 2015). Furthermore, SAT and OHC responses to increased volcanic emissions, a succession of solar minima, and

decreased greenhouse gases are all characterized by cooling in the tropical Pacific in the simulations presented here. The volcanic response appears more consistent with a direct thermal response to reduced radiative forcing than a dynamical response, as described by Emile-Geay et al. (2008). TSI increases in this region have been shown to trigger La Niña–like conditions initially (Emile-Geay et al. 2007), followed by lagged ENSO-like conditions (Meehl and Arblaster 2009). These results provide few constraints on the multidecadal TSI responses detected in this study. Finally, the GHG response appears consistent with dynamical responses to greenhouse gases (Wang et al. 2013). It is important to recognize that even the large changes in radiative forcings between glacial and interglacial periods severely test the ability of a given coupled model to adequately represent the subtle atmosphere–ocean interaction that is at the heart of the ENSO phenomenon (e.g., see Peltier and Solheim 2004; Vettoretti et al. 2009).

The perturbation OHC responses in the NAtl are only significant with respect to the NO_VOLC experiment in a band along the eastern boundary, although the fully transient OHC changes there are very large across the NAtl. This result suggests that the NAtl OHC reductions are either not easily separable from internal variability or are themselves generated by internal variability. The latter explanation is contradicted by two different facts. First, the amplitude of the fully transient signal exceeds the 95% confidence range of internal variability fluctuations in this region from the control simulations. Second, the sign and amplitude of the NAtl OHC reductions are similar in every ensemble member examined here. Instead, this feature resembles an AMO response associated with a reduction in the AMOC. Indeed, we find that the AMOC decreases from the MCA to the LIA by 0.5 and 0.4 Sv (1 Sv ≡ $10^6 \, m^3 \, s^{-1}$; $p < 0.05$ with respect to control variations) for the T42 and T85 simulations, respectively. Such reductions in both the AMOC and AMO over the last millennium have also been reconstructed from observations (Wanamaker et al. 2012). However, because of the large variability in AMOC values over the last millennium (not shown), particularly for the T42 simulations, it is difficult to separate the influences of different forcings in driving these AMOC changes.

The Arctic amplification of cooling from the MCA to the LIA presented here is consistent with reconstructions and other PMIP3 simulations (Wang et al. 2015). In the fully transient T85 simulations, the Barents Sea includes the region of strongest SAT decrease, strong sea ice increase, and significant OHC increase. Such a combination of effects can be explained by sea ice growth in the Barents Sea preventing the transfer of heat from the ocean to the atmosphere (Zhong et al. 2011; Lehner et al. 2013). Such sea ice changes have been found previously to trigger a set of feedbacks resulting in the reduction of the AMOC and decreased heat transport into the Arctic in other T42 simulations with CCSM3 (Zhong et al. 2011; Lehner et al. 2013), although the relationship between sea ice expansion and the AMOC depended on the background conditions of each simulation (Zhong et al. 2011). Arctic SAT responses at T42 resolution are similar to those at T85 resolution, but Arctic OHC at T42 resolution reduces much more strongly over the entire Arctic Basin than at T85 resolution. Arctic sea ice growth is also much less extensive at T42 resolution than at T85. The AMOC at T42 resolution (not shown) is also characterized more by centennial-time-scale oscillations than by a gradual decrease, as found in the T85 simulations.

One explanation for the dependence on resolution in Arctic sea ice concentration and OHC changes is the large difference in mean climate states between simulations at these two resolutions (Andres and Peltier 2013). Arctic SATs are approximately 2°C colder in CCSM3 T42-resolution simulations than in T85 simulations (deWeaver and Bitz 2006; Hack et al. 2006). Consequently, Arctic sea ice is initially more extensive at T42 resolution than T85 (deWeaver and Bitz 2006), with values of approximately $17.5 \times 10^{12} \, m^2$ for the T42 control simulation in this study and approximately $16.5 \times 10^{12} \, m^2$ in the T85 control simulation. These differences in background state explain the smaller increases in sea ice concentration detected here at T42 resolution and the smaller change in Arctic SATs. Since the Arctic SATs are biased high with respect to observations at both resolutions (Grotjahn et al. 2011), it is reasonable to expect that the sea ice and SAT changes detected in the T42 simulation would be closer to historical values than in the T85 simulation.

The pressure biases that generate the Arctic SAT and sea ice extent biases in CCSM3 also lead to dynamical differences between simulations of a different resolution and between them and observations (deWeaver and Bitz 2006). In a previous study with CCSM3 in a T42 configuration, Arctic summer winds were found to generate a polar anticyclone instead of the polar cyclone observed in reanalysis products (deWeaver and Bitz 2006). This may not indicate a poor representation of Arctic dynamics, however, since historical circulation patterns in the Arctic Basin suggest that circulation regimes switch between these two states periodically (Proshutinsky et al. 2015). In contrast, simulations at a T85 resolution exhibit no coherent summer wind structures (deWeaver and Bitz 2006). Thus, through a

combination of background climate biases between simulations at the two resolutions, large differences in the Arctic SAT, OHC, and sea ice responses to external forcings are generated.

Some of the mechanisms described above involve nonlinear responses to the external climate forcings. The main sources of nonlinearity present in the regions discussed here are listed:

(i) The small number of ensemble members employed in estimating the degree of nonlinearity and the examination of small spatial regions allows discrepancies between the fully transient changes and the linear combination of changes to be strongly affected by noise from local phenomena in many grid cells. However, the range of such noise is captured in the control simulation confidence intervals.

(ii) Modes of variability can amplify or reduce the influence of one or more forcings. For example, the AMO varies on time scales similar to the length of the short MCA and short LIA. Random fluctuations in the AMO may obscure a forcing response change between these two periods entirely, but ensemble averages reduce the effect of such random events. On the other hand, if an AMO reduction were triggered by feedbacks associated with forcing responses in the Barents Sea, then the amplitude of the response in the North Atlantic may be nonlinearly related to the initial forcing. In Fig. 6b, there is no evidence of significant nonlinearity in the North Atlantic. Thus, if such an AMO response were occurring, its amplitude must remain within the range of natural variability.

(iii) Other feedbacks can also amplify or reduce signals locally and, if they involve teleconnections, may affect remote regions as well. Additionally, some feedback processes (including sea ice formation and melting, or snow deposition) are sensitive to the background conditions at the time of the forcing (Berdahl and Robock 2013). In this study, nonlinearities are detected in sea ice concentration changes in regions where sea ice was not originally present. All of the forcings examined here are seen to contribute to the sea ice changes, most probably by lowering the mean SATs in those regions to be closer to the threshold temperatures for sea ice formation.

(iv) Ocean and atmospheric circulation may advect seawater or air whose state has been altered in response to the forcing into other regions, where it can affect ambient conditions. In Mignot et al. (2011), large volcanic eruptions first cause strong reductions in tropical ocean temperatures with weaker responses in the midlatitudes. After at least a year, temperature anomalies in the midlatitudes strengthen in response to the advection of the anomalously cold tropical water.

Given the nonlinearities detected in the forcing responses here, these results challenge the assumption that attribution studies based on varying a single parameter at a time will arrive at the same results as a study where forcings are removed one at a time.

5. Conclusions

Through a suite of last millennium simulations and perturbation experiments using a single climate model, the roles of external forcings in generating regional climate changes from the MCA to the LIA have been assessed. In these simulations, the immediate NH SAT responses to large volcanic eruptions exceed that predicted by Mann et al. (2009), whereas the amplitude of the transition from the MCA to the LIA was found to be weaker than in the Mann et al. (2009) reconstruction. These characteristics are, however, similar to those from other last millennium simulations (e.g., Berdahl and Robock 2013; Bothe et al. 2013) and lie within the range spanned by different reconstruction methods (Wang et al. 2015). The analyses presented here demonstrate that the transition from the MCA to the LIA is generally associated with decreasing SATs and OHC and increases in sea ice concentrations. SAT reductions are strongest in the Barents Sea, with strong reductions over the Arctic and northwestern Europe. OHC reductions are strongest in the midlatitudes, particularly in the NAtl. Sea ice concentrations increase over most of its extent, but these increases are strongest over the Barents Sea and the Bering Strait.

Resolution differences are detected in the predicted changes from the MCA to the LIA for all variables discussed. Arctic SAT reductions and sea ice concentration increases are stronger at T85 resolution than T42, and OHC reductions over most of the NH are stronger at T42 resolution than T85. In the Arctic Basin, resolution differences are hypothesized to be associated with differences in the background climate state generated by the model. As such, these differences may be particular to CCSM3. As a result of such particularities in any one model, the representativeness of the results presented here can only be assessed by repeating similar experiments with other models.

Both volcanic and TSI forcings are important to changes from the short MCA to the LIA by generating SAT and OHC reductions in the tropical Pacific and

increases in sea ice extent at the sea ice margins. At T85 resolution, these forcings are also associated with strong reductions in SAT and increases in sea ice concentration in the Barents Sea.

In contrast, GHG and orbital forcings generate fewer significant responses from the MCA to the LIA. GHGs are associated with SAT decreases in the tropical Pacific, and both forcings are associated with sea ice concentration increases in the Norwegian Sea and the Gulf of Alaska. Analyzing a single perturbation simulation in the NO_GHG and NO_ORBIT experiments is seen to be insufficient to isolate these forced signals from the unforced signals in many cases, given the slow time scales of variations associated with both forcings and the large amplitude of multidecadal and longer variations in the T42 simulations. Additionally, the LIA includes periods of both low and high GHG forcings, which makes its responses weaker than when examined over a shorter period of low forcing.

Nonlinearities in the forcing responses are detected along sea ice margins in the western tropical Pacific and in North Africa and central Eurasia. These nonlinearities indicate sensitivity to background conditions or the other forcings being applied when assessing a given forcing response. As such, they must be considered when designing attribution experiments.

APPENDIX A

Correcting for Disequilibration in Fully Transient Simulations

Three equilibration criteria were applied to the control simulations (Andres and Peltier 2013):

1) Mean net top-of-atmosphere radiation fluxes remain within $\pm 0.1 \, \text{W m}^{-2}$ over the last 200 years.
2) Net top-of-atmosphere radiation fluxes display insignificant trends over the last 200 years.
3) Globally averaged surface temperatures display insignificant trends over the last 200 years.

The equilibration period included 2090 and 1300 years for the T42 and T85 control simulations, respectively (Andres and Peltier 2013). Ensemble averages over transient simulations at each resolution are plotted in Fig. A1 for globally averaged SATs and globally summed OHC, NH sea ice extent, and AMOC. Third-order polynomials are fit to global changes extracted from the control simulations at each resolution by minimizing least squares differences. They are also plotted in Fig. A1, with gray shaded regions indicating confidence ranges for a future measurement. The order of the polynomial was chosen to be the lowest value that captures the multicentennial trends in the data for all variables.

Globally averaged SATs appear to be well equilibrated at both resolutions, as the control time series show little variation. AMOC variations in the transient simulations lie within the 95% confidence bounds of the corresponding control datasets until the very end of the millennium. Sea ice extent variations generally exceed variations extracted from the control simulations during the second half of the millennium, particularly for T85 resolution, but show little variation on centennial time scales prior to that. In contrast, global OHC exhibits noticeable trends over the early part of the millennium at both resolutions, and variations in the values from T42 resolution coincide with changes in the control simulation. This effect is less pronounced at T85 resolution. Thus, there appears to be lingering disequilibrium in the deep ocean of the millennium simulations that is primarily affecting variations in ocean variables during at least the early part of the preindustrial millennium. We conclude that basing the equilibration criteria solely on surface variables and top-of-atmosphere radiation fluxes is insufficient to ensure full equilibration of the deep ocean.

To separate the effects of disequilibrium from those due to transient forcings, third-order polynomial fits to control simulation variables are subtracted from transient simulation variables prior to any analyses presented here. For maps, the corrections are applied separately in every grid cell to polynomials generated from the same grid cell. Polynomial fits to regional averages are calculated after the control simulation data have been regionally averaged.

Note that the first 550 years of the equilibrated T85-resolution control sea ice data and years 350–550 of ocean data were irretrievably lost. Since the ocean data losses are located in the middle of the time series and constitute less than 1 degree of freedom of the third-order polynomial time series, they can be effectively interpolated over using the polynomial fit. However, the sea ice data loss cannot be extrapolated as
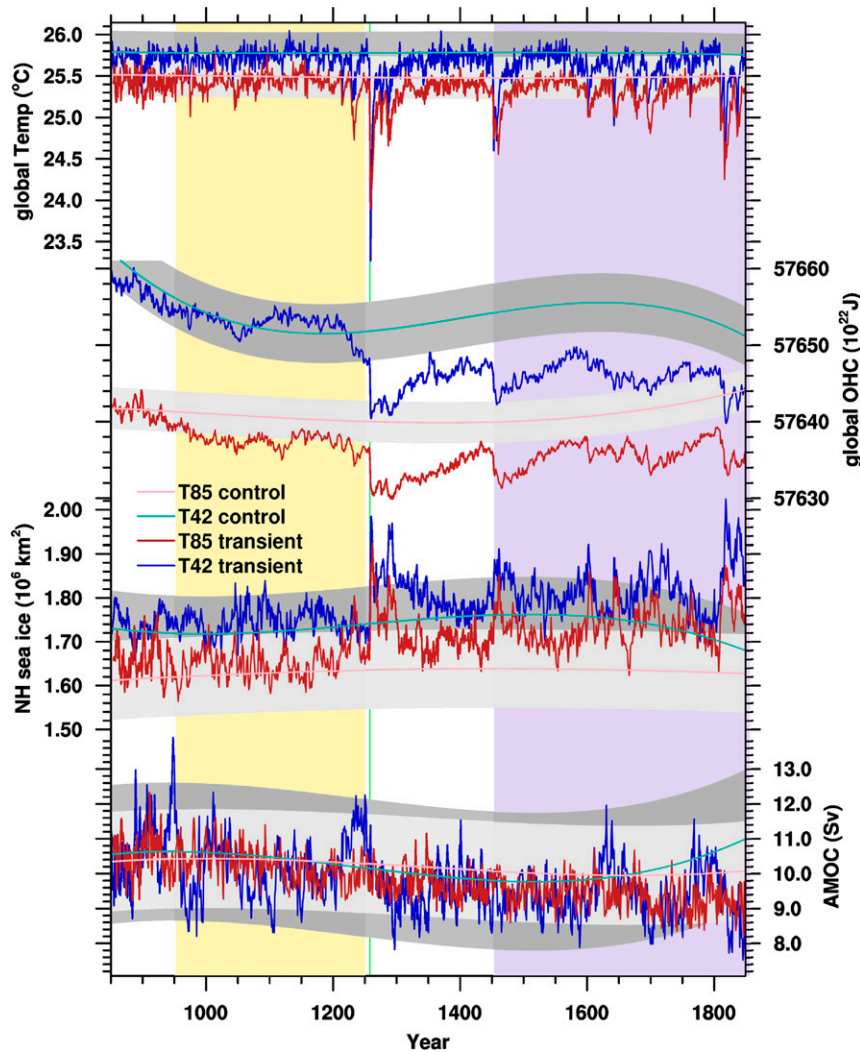
FIG. A1. Globally averaged SAT, globally summed OHC, NH sea ice extent, and AMOC for fully transient preindustrial millennium simulations at each resolution aligned with respect to their initialization dates. Third-order polynomials extracted from corresponding years in the control simulations are also presented, with gray shading indicating the 95% confidence intervals for future predictions. The yellow-shaded region corresponds to the Medieval Climate Anomaly, and the purple-shaded region corresponds with the Little Ice Age. A vertical green line indicates the timing of the Samalas volcanic event.

effectively. This is seen in the blue curve of Fig. A2, where the polynomial fit to years with complete data yields very large extrapolated values for the early part of the millennium. However, sea ice data for the end of December are available every 10 years as part of the model restart output. These data prove to be sufficient to reproduce roughly two-thirds of the variability ($R^2 = 0.67$) of annually averaged data during overlap years, and they are also highly correlated with annual average variations during those years ($r = 0.8$). Thus, a hybrid T85-resolution control sea ice dataset is constructed

including annually averaged data for years with complete cover and decadal reconstructions for the remaining years. The polynomial fit based on the hybrid dataset is shown in the red curve of Fig. A2 and is also plotted as the T85-resolution control time series for sea ice in Fig. A1. Including the reconstructed annual data aligns the estimates of T85-resolution control sea ice extent over the early part of the millennium much more closely with averages from the transient T85 simulations. Thus, this reconstruction is employed for all of the sea ice corrections.
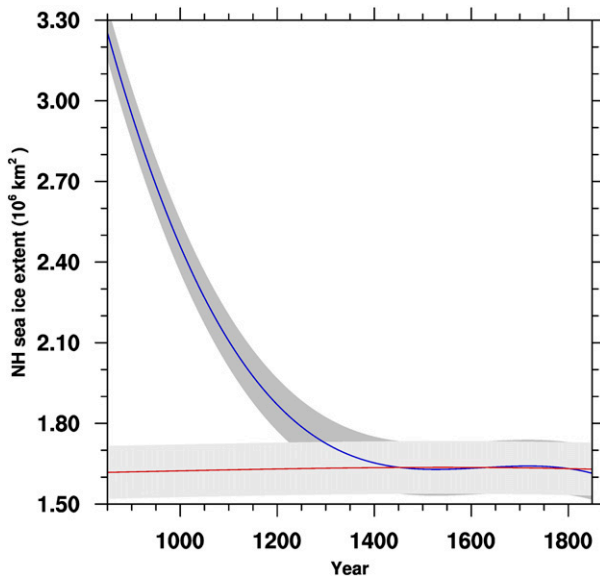
FIG. A2. Polynomial fit to Mill_T85_ctl NH sea ice extent time series based on all available complete years (blue) and including available restart data regressed onto annual values (red).

APPENDIX B

Defining Confidence Intervals Based on Control Data

Confidence intervals are defined using bootstrapping methods with control data in such a way as to reproduce the analysis methods employed. For maps of fully transient changes from the MCA to the LIA (or from the short MCA to the short LIA), the polynomial fit to control data is subtracted from the control time series in order to reproduce the equilibration correction. The start dates of MCA and LIA periods are randomly selected from within the control run time series, and then segments of a corresponding length of time are extracted. Selecting segments of control data rather than randomly selecting every data point maintains time series autocorrelations. Then the differences between the averages of these two periods are evaluated. Over 2000 separate samples are generated, from which ensemble averages over as many difference maps as transient time series are calculated. Finally, in every grid cell, the 2.5th and 97.5th percentiles are identified to form the lower and upper limits of the confidence interval. Thus, statistically significant signals are identified against a background of unforced climate variability.

Confidence intervals for the perturbation difference maps are generated in a similar manner. Since no equilibration correction is applied to these time series in the analyses presented, uncorrected control data are employed for those confidence intervals. Then, prior to ensemble averaging, differences between sets of two bootstrapped MCA–LIA changes are calculated.

Finally, confidence intervals are also defined for the difference between linear combinations and fully transient changes between the short MCA and short LIA. In this case, sums over sets of four difference maps are generated to reproduce the linear combination of perturbation signals, and differences are calculated between these maps and randomly selected MCA–LIA changes. Since the NO_GHG and NO_ORBIT perturbation differences are identical for both Mill_T42_all_Gao and Mill_T42_all_Crowley, sets of two linear combination differences are generated with two of the four difference maps being identical. Averages are performed over the sets.

REFERENCES

Andres, H. J., and W. R. Peltier, 2013: Examining internal and external contributors to Greenland climate variability using CCSM3. *J. Climate*, **26**, 9745–9773, doi:10.1175/JCLI-D-12-00845.1.

——, and ——, 2015: Attributing observed Greenland responses to natural and anthropogenic climate forcings. *Climate Dyn.*, **45**, 2919–2936, doi:10.1007/s00382-015-2514-4.

Berdahl, M., and A. Robock, 2013: Northern Hemispheric cryosphere response to volcanic eruptions in the Paleoclimate Modeling Intercomparison Project 3 last millennium simulations. *J. Geophys. Res.*, **118**, 12 359–12 370, doi:10.1002/2013JD019914.

Berger, A. L., 1978: Long-term variations of daily insolation and quaternary climatic changes. *J. Atmos. Sci.*, **35**, 2362–2367, doi:10.1175/1520-0469(1978)035<2362:LTVODI>2.0.CO;2.

Bothe, O., J. H. Jungclaus, and D. Zanchettin, 2013: Consistency of the multi-model CMIP5/PMIP3-past1000 ensemble. *Climate Past*, **9**, 2471–2487, doi:10.5194/cp-9-2471-2013.

Church, J. A., N. J. White, and J. M. Arblaster, 2005: Significant decadal-scale impact of volcanic eruptions on sea level and ocean heat content. *Nature*, **438**, 74–77, doi:10.1038/nature04237.

Collins, W., and Coauthors, 2006: The Community Climate System Model version 3 (CCSM3). *J. Climate*, **19**, 2122–2143, doi:10.1175/JCLI3761.1.

Crowley, T., G. Zielinski, B. Vinther, R. Udisti, K. Kreutz, J. Cole-Dai, and E. Castellano, 2008: Volcanism and the Little Ice Age. *PAGES Newsletter*, Vol. 16, PAGES International Project Office, Bern, Switzerland, 22–23.

Cunningham, L. K., and Coauthors, 2013: Reconstructions of surface ocean conditions from the northeast Atlantic and Nordic seas during the last millennium. *Holocene*, **23**, 921–935, doi:10.1177/0959683613479677.

deWeaver, E., and C. Bitz, 2006: Atmospheric circulation and its effect on Arctic sea ice in CCSM3 simulations at medium and high resolution. *J. Climate*, **19**, 2415–2436, doi:10.1175/JCLI3753.1.

Emile-Geay, J., M. Cane, R. Seager, A. Kaplan, and P. Almasi, 2007: El Niño as a mediator of the solar influence on climate. *Paleoceanography*, **22**, PA3210, doi:10.1029/2006PA001304.

——, R. Seager, M. A. Cane, E. R. Cook, and G. H. Haug, 2008: Volcanoes and ENSO over the past millennium. *J. Climate*, **21**, 3134–3148, doi:10.1175/2007JCLI1884.1.

Fernandez-Donado, L., and Coauthors, 2013: Large-scale temperature response to external forcing in simulations and reconstruction of the last millennium. *Climate Past*, **9**, 393–421, doi:10.5194/cp-9-393-2013.

Gao, C., A. Robock, and C. Ammann, 2008: Volcanic forcing of climate over the past 1500 years: An improved ice core-based index for climate models. *J. Geophys. Res.*, **113**, D23111, doi:10.1029/2008JD010239.

Gennaretti, F., D. Arsenault, A. Nicault, L. Perreault, and Y. Begin, 2014: Volcano-induced regime shifts in millennial tree-ring chronologies from northeastern North America. *Proc. Natl. Acad. Sci. USA*, **111**, 10 077–10 082, doi:10.1073/pnas.1324220111.

Gent, P. R., and Coauthors, 2011: The Community Climate System Model version 4. *J. Climate*, **24**, 4973–4991, doi:10.1175/2011JCLI4083.1.

Gregory, J. M., J. A. Lowe, and S. F. B. Tett, 2006: Simulated global-mean sea level changes over the last half-millennium. *J. Climate*, **19**, 4576–4589, doi:10.1175/JCLI3881.1.

Grotjahn, R., L.-L. Pan, and J. Tribbia, 2011: CAM3 bias over the Arctic region during northern winter studied with a linear stationary model. *Climate Dyn.*, **37**, 631–645, doi:10.1007/s00382-011-1033-1.

Hack, J. J., J. M. Caron, G. Danabasoglu, K. W. Oleson, C. Bitz, and J. E. Truesdale, 2006: CCSM–CAM3 climate simulation sensitivity to changes in horizontal resolution. *J. Climate*, **19**, 2267–2289, doi:10.1175/JCLI3764.1.

Hanhijarvi, S., M. P. Tingley, and A. Korhola, 2013: Pairwise comparisons to reconstruct mean temperature in the Arctic Atlantic region over the last 2,000 years. *Climate Dyn.*, **41**, 2039–2060, doi:10.1007/s00382-013-1701-4.

Iwi, A. M., L. Hermanson, K. Haines, and R. T. Sutton, 2012: Mechanisms linking volcanic aerosols to the Atlantic meridional overturning circulation. *J. Climate*, **25**, 3039–3051, doi:10.1175/2011JCLI4067.1.

Joos, F., and R. Spahni, 2008: Rates of change in natural and anthropogenic radiative forcing over the past 20,000 years. *Proc. Natl. Acad. Sci. USA*, **105**, 1425–1430, doi:10.1073/pnas.0707386105.

Kaufman, D. S., and Coauthors, 2009: Recent warming reverses long-term Arctic cooling. *Science*, **325**, 1236–1239, doi:10.1126/science.1173983.

Landrum, L., B. L. Otto-Bliesner, E. R. Wahl, A. Conley, P. J. Lawrence, N. Rosenbloom, and H. Teng, 2013: Last millennium climate and its variability in CCSM4. *J. Climate*, **26**, 1085–1111, doi:10.1175/JCLI-D-11-00326.1.

Lavigne, F., and Coauthors, 2013: Source of the great A.D. 1257 mystery eruption unveiled, Samalas volcano, Rinjani Volcanic Complex, Indonesia. *Proc. Natl. Acad. Sci. USA*, **110**, 16 742–16 747, doi:10.1073/pnas.1307520110.

Lehner, F., A. Born, C. C. Raible, and T. F. Stocker, 2013: Amplified inception of European Little Ice Age by sea ice–ocean–atmosphere feedbacks. *J. Climate*, **26**, 7586–7602, doi:10.1175/JCLI-D-12-00690.1.

Mann, M. E., and Coauthors, 2009: Global signatures and dynamical origins of the Little Ice Age and Medieval Climate Anomaly. *Science*, **326**, 1256–1260, doi:10.1126/science.1177303.

Masson-Delmotte, V., and Coauthors, 2013: Information from paleoclimate archives. *Climate Change 2013: The Physical Science Basis*, T. F. Stocker et al., Eds., Cambridge University Press, 383–464.

McGregor, H. V., and Coauthors, 2015: Robust global ocean cooling trend for the pre-industrial Common Era. *Nat. Geosci.*, **8**, 671–677, doi:10.1038/ngeo2510.

Meehl, G. A., and J. M. Arblaster, 2009: A lagged warm event–like response to peaks in solar forcing in the Pacific region. *J. Climate*, **22**, 3647–3660, doi:10.1175/2009JCLI2619.1.

Mignot, J., M. Khodri, C. Frankignoul, and J. Servonnat, 2011: Volcanic impact on the Atlantic Ocean over the last millennium. *Climate Past*, **7**, 1439–1455, doi:10.5194/cp-7-1439-2011.

Miller, G. H., and Coauthors, 2012: Abrupt onset of the Little Ice Age triggered by volcanism and sustained by sea-ice/ocean feedbacks. *Geophys. Res. Lett.*, **39**, L02708, doi:10.1029/2011GL050168.

PAGES 2k Consortium, 2013: Continental-scale temperature variability during the past two millennia. *Nat. Geosci.*, **6**, 339–347, doi:10.1038/NGEO1797.

Peltier, W. R., and L. P. Solheim, 2004: The climate of the Earth at Last Glacial Maximum: Statistical equilibrium state and a mode of internal variability. *Quat. Sci. Rev.*, **23**, 335–357, doi:10.1016/j.quascirev.2003.07.003.

Phipps, S. J., and Coauthors, 2013: Paleoclimate data–model comparison and the role of climate forcings over the past 1500 years. *J. Climate*, **26**, 6915–6936, doi:10.1175/JCLI-D-12-00108.1.

Proshutinsky, A., D. Dukhovskoy, M.-L. Timmermans, R. Krishfield, and J. L. Bamber, 2015: Arctic circulation regimes. *Philos. Trans. Roy. Soc.*, **A373**, 20140160, doi:10.1098/rsta.2014.0160.

Schleussner, C. F., and G. Feulner, 2013: A volcanically triggered regime shift in the subpolar North Atlantic Ocean as a possible origin of the Little Ice Age. *Climate Past*, **9**, 1321–1330, doi:10.5194/cp-9-1321-2013.

Schmidt, G., and Coauthors, 2011: Climate forcing reconstructions for use in PMIP simulations of the last millennium (v1.0). *Geosci. Model Dev.*, **4**, 33–45, doi:10.5194/gmd-4-33-2011.

——, and Coauthors, 2012: Climate forcing reconstructions for use in PMIP simulations of the last millennium (v1.1). *Geosci. Model Dev.*, **5**, 185–191, doi:10.5194/gmd-5-185-2012.

Schurer, A. P., G. C. Hegerl, M. E. Mann, S. F. B. Tett, and S. J. Phipps, 2013: Separating forced from chaotic climate variability over the past millennium. *J. Climate*, **26**, 6954–6973, doi:10.1175/JCLI-D-12-00826.1.

——, S. F. B. Tett, and G. C. Hegerl, 2014: Small influence of solar variability on climate over the past millennium. *Nat. Geosci.*, **7**, 104–108, doi:10.1038/ngeo2040.

Servonnat, J., P. Yiou, M. Khodri, D. Swingedouw, and S. Denvil, 2010: Influence of solar variability, CO_2 and orbital forcing between 1000 and 1850 AD in the IPSLCM4 model. *Climate Past*, **6**, 445–460, doi:10.5194/cp-6-445-2010.

Timmreck, C., S. Lorenz, T. Crowley, S. Kinne, T. Raddatz, M. Thomas, and J. Jungclaus, 2009: Limited temperature response to the very large AD 1258 volcanic eruption. *Geophys. Res. Lett.*, **36**, L21708, doi:10.1029/2009GL040083.

——, H.-F. Graf, S. Lorenz, U. Niemeier, D. Zanchettin, D. Matei, J. Jungclaus, and T. Crowley, 2010: Aerosol size confines climate response to volcanic super-eruptions. *Geophys. Res. Lett.*, **37**, L24705, doi:10.1029/2010GL045464.

Trouet, V., J. Esper, N. E. Graham, A. Baker, J. D. Scourse, and D. C. Frank, 2009: Persistent positive North Atlantic Oscillation mode dominated the Medieval Climate Anomaly. *Science*, **324**, 78–80, doi:10.1126/science.1166349.

Tulloch, R., and J. Marshall, 2012: Exploring mechanisms of variability and predictability of Atlantic meridional overturning circulation in two coupled climate models. *J. Climate*, **25**, 4067–4080, doi:10.1175/JCLI-D-11-00460.1.

van Loon, H., and G. A. Meehl, 2008: The response in the Pacific to the sun's decadal peaks and contrasts to cold events in the Southern Oscillation. *J. Atmos. Sol. Terr. Phys.*, **70**, 1046–1055, doi:10.1016/j.jastp.2008.01.009.

Vettoretti, G., M. D'Orgeville, and W. R. Peltier, 2009: Polar climate instability and climate teleconnections from the Arctic to the midlatitudes and tropics. *J. Climate*, **22**, 3513–3539, doi:10.1175/2009JCLI2481.1.

Vieira, L., S. Solanki, N. Krivova, and I. Usoskin, 2011: Evolution of the solar irradiance during the holocene. *Astron. Astrophys.*, **531**, A6, doi:10.1051/0004-6361/201015843.

Wanamaker, A. D., Jr., P. G. Butler, J. D. Scourse, J. Heinemeier, J. Eiriksson, K. L. Knudsen, and C. A. Richardson, 2012: Surface changes in the North Atlantic meridional overturning circulation during the last millennium. *Nat. Commun.*, **3**, 899, doi:10.1038/ncomms1901.

Wang, J., J. Emile-Geay, D. Guillot, N. P. McKay, and B. Rajaratnam, 2015: Fragility of reconstructed temperature patterns over the Common Era: Implications for model evaluation. *Geophys. Res. Lett.*, **42**, 7162–7170, doi:10.1002/2015GL065265.

Wang, S.-Y., M. L'Heureux, and J.-H. Yoon, 2013: Are greenhouse gases changing ENSO precursors in the western North Pacific? *J. Climate*, **26**, 6309–6322, doi:10.1175/JCLI-D-12-00360.1.

Zhong, Y., G. H. Miller, B. L. Otto-Bliesner, M. M. Holland, D. A. Bailey, D. P. Schneider, and A. Geirsdottir, 2011: Centennial-scale climate change from decadally-paced explosive volcanism: A coupled sea ice-ocean mechanism. *Climate Dyn.*, **37**, 2373–2387, doi:10.1007/s00382-010-0967-z.